INTERNATIONAL JOURNAL FOR NUMERICAL METHODS IN FLUIDS, VOL. 24, 141–153 (1997)

A NON-OSCILLATORY NO-FREE-PARAMETER FINITE ELEMENT ALGORITHM AND ITS APPLICATIONS IN CFD

YAN WANG AND BING-GANG TONG
Graduate School, University of Science and Technology of China, PO Box 3908, Beijing 100039, People's Republic of China
AND
GUI-QING JIANG AND XIAO-MIN WANG
Beijing Institute of Aerodynamics, PO Box 7215, Beijing 100074, People's Republic of China

SUMMARY

A non-oscillatory no-free-parameter finite element method (NNFEM) is presented based on the consideration of wave propagation characteristic in different characteristic directions across a strong discontinuity through flux vector splitting in order to satisfy the increasing entropy condition. The algorithm is analysed in detail for the one-dimensional (1D) Euler equation and then extended to the 2D, axisymmetric and 3D Euler and Navier–Stokes equations. Its applications in various cases—inviscid oblique shock wave reflection, flow over a forward step, axisymmetric free jet flow, supersonic flows over 2D and 3D rectangular cavities—are given. These computational results show that the present NNFEM is efficient in practice and stable in operations and is especially capable of giving good resolution in simulating complicated separated and vortical flows interacting with shock waves.

KEY WORDS: finite element; non-oscillatory; strong discontinuity

1. INTRODUCTION

The development of the finite element technique and its extensive applications in CFD has attracted more and more researchers in recent decades. One of its main difficulties is how to get high-resolution computations in shock wave regions and also in complicated viscous flow fields. In comparison with the success of high-resolution finite difference schemes such as TVD[1] and NND,[2] some advances have been achieved in finite element algorithms. The streamline upwind Petrov–Galerkin (SUPG) algorithm of Hughes and Mallet[3] and the ENO discretized algorithm of Baker and Kim[4] can eliminate the spurious oscillations in simulating shock waves, but their computational resolution across shock waves is still unsatisfactory. Remakrishman *et al.*[5] increased the computational resolution in the shock wave region by adding artificial viscosity in the discretization and using the mesh refinement or mesh self-adaptation technique, but were not very successful in practice and still worried about the existence of spurious oscillations. The failure of the finite element method in this respect seriously retards its ability to successfully simulate complex supersonic/hypersonic flow problems.

Referring to an idea used in the finite difference method,[2] we propose here a non-oscillatory no-free parameter finite element method (NNFEM) based on the consideration of wave propagation

CCC 0271–2091/97/020141–13

Received August 1995
Revised March 1996

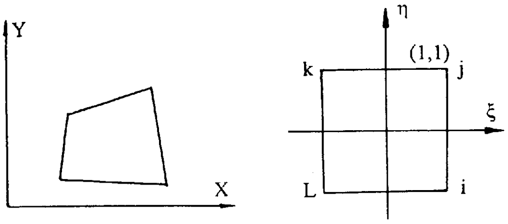

Figure 1. 2D element co-ordinate transformation

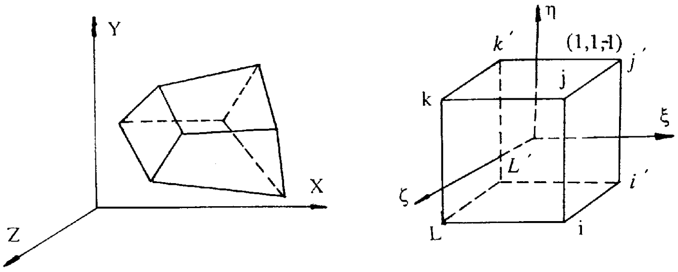

Figure 2. 3D element co-ordinate transformation

characteristic in different characteristic directions across a strong discontinuity through flux vector splitting in order to satisfy the increasing entropy condition. For verification of the present algorithm an inviscid oblique shock wave reflection and a supersonic flow over a forward step are computed and compared with available results. Also, an axisymmetric free jet flow with a high pressure ratio is computed, where a Mach disc and a drum-like shock wave have been clearly shown. Next, supersonic flows over 2D and 3D rectangular cavities are successfully simulated, where periodic motions of shock waves and vortex flows have been investigated.

In Section 2, we introduce the present algorithm in the discretization of the 1D Euler equation. Then it is extended to discretize the 2D, axisymmetric and 3D Euler equations in Section 3. In Section 4 several applications and discussions are given. Finally, conclusions are presented in Section 5.

2. NNFEM IN DISCRETIZATION OF 1D EULER EQUATIONS

The 1D Euler equation has the form

$$\frac{\partial U}{\partial t}+\frac{\partial F}{\partial x}=0,$$

$$U=\begin{bmatrix}\rho\\ \rho u\\ e\end{bmatrix},\qquad F=\begin{bmatrix}\rho u\\ \rho u^2+p\\ (e+p)u\end{bmatrix}, \tag{1}$$

where u, ρ, p and e denote velocity, density, pressure and total specific energy respectively. Now equation (1) can be discretized by the Galerkin weighted residual method and integrated using Green's formula. For every element e we have

$$\int_e [N][N]^{\mathrm{T}}\,\mathrm{d}x\left[\frac{\partial u}{\partial t}\right]=\int_e \frac{\partial[N]}{\partial x}F\,\mathrm{d}x+\text{boundary conditions}. \tag{2}$$

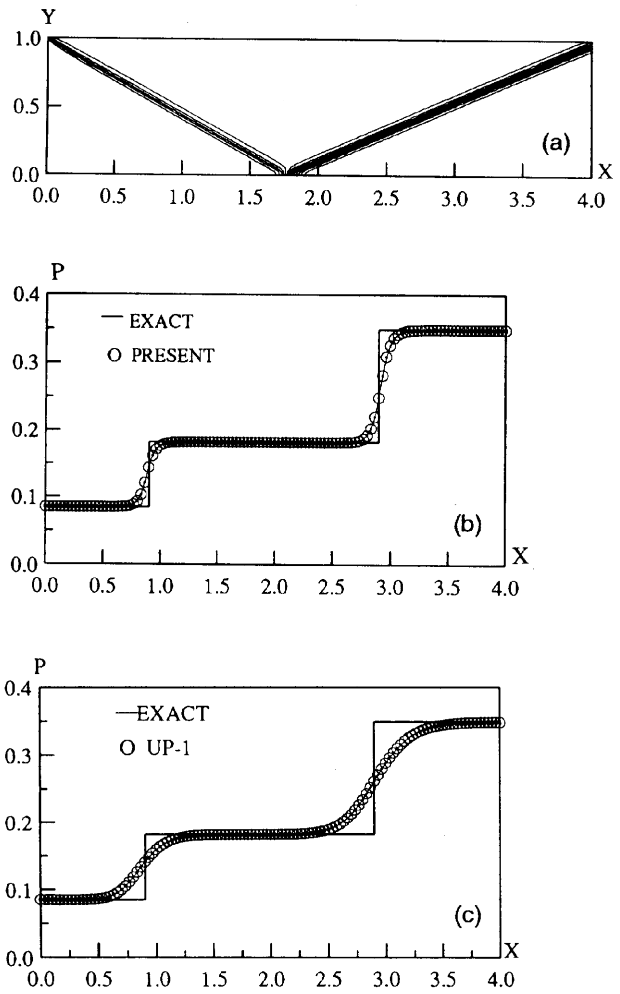

Figure 3. Computed results for the inviscid shock wave reflection with incident shock angle $\phi = 29^\circ$, stream Mach number 2·9 and uniform isotropic grid 121 × 31: (a) computed pressure contours by present algorithm; (b) computed pressure distribution along grid line on $y = 0{\cdot}5$ by present algorithm; (c) computed pressure distribution along grid line on $y = 0{\cdot}5$ by first-order upwind scheme

In the classic Galerkin finite element method, the flux vector F is approximated linearly as

$$F = N_i F_i + N_j F_j,$$

$$N_i = (x_j - x)/(x_j - x_i), \qquad N_j = (x - x_i)/(x_j - x_i),$$

where i and j denote the nodes of the element e. This expression leads to the spurious oscillations across a strong discontinuity, otherwise an artificial viscosity is needed.

Now we attack the problem physically. First, according to the different characteristic directions, F is split by Steger's technique[6] into positive and negative fluxes so that the following hold.

(i) $F = AU$, i.e. F is a homogeneous function of U.

(ii) The Jacobian matrix A may be written as

$$A = \partial F/\partial U = S^{-1}\Lambda S,$$

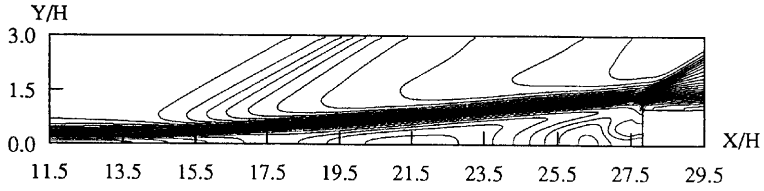

Figure 4. Density contours of 2D forward step

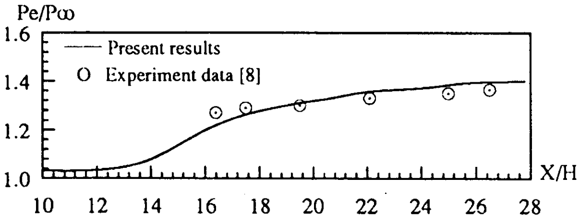

Figure 5. Pressure distribution along wall for 2D forward step

where S is a non-singular characteristic vector. If λ_i denote the characteristic roots of A, then

$$\Lambda = \mathrm{diag}\{\lambda_i\}, \qquad i = 1, 2, 3.$$

(iii) By using Steger's splitting technique,

$$\Lambda^{\pm} = \mathrm{diag}\left\{\frac{\lambda_i \pm |\lambda_i|}{2}\right\}, \qquad i = 1, 2, 3.$$

(iv) We get $F^{\pm} = S^{-1}\Lambda^{\pm}SU = A^{\pm}U, F = F^{+} + F^{-}$.

Up to now it is clear that for F^{+} the waves propagate from the upstream to the downstream and reversely for F^{-}. We can simulate this by using the forward and backward finite difference technique. Hence F^{+} and F^{-} in the element e may be expressed with forward and backward Taylor series expansions respectively up to second-order accuracy as

$$F_e^{+}(x) = F_i^{+} + (x - x_i)\left(\frac{\partial F^{+}}{\partial x}\right)_i + O(\Delta x^2), \qquad F_e^{-}(x) = F_i^{-} + (x - x_j)\left(\frac{\partial F^{-}}{\partial x}\right)_j + O(\Delta x^2), \tag{3}$$

$$\left(\frac{\partial F^{+}}{\partial x}\right)_i = \frac{F_j^{+} - F_i^{+}}{\Delta x} + O(\Delta x), \qquad \left(\frac{\partial F^{-}}{\partial x}\right)_j = \frac{F_j^{-} - F_i^{-}}{\Delta x} + O(\Delta x). \tag{4}$$

In order to eliminate spurious oscillations across the shock wave, according to the analysis made for the construction of the NND scheme,[2] each derivative in (3) should be taken to be one, which absolute value is the minimum between those on nodes i and j. If the signs of these derivatives on i and j are different, we just take the minimum value to be zero. If the symbol **minmod** is used, i.e.

$$\mathbf{minmod}(a, b) = 0{\cdot}5\ [\mathbf{sign}(a) + \mathbf{sign}(b)]\mathbf{min}(|a|, |b|),$$

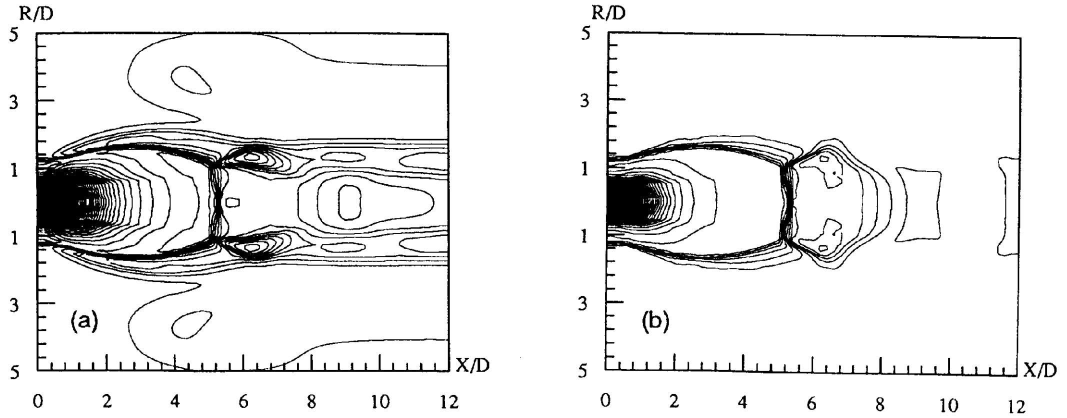

Figure 6. (a) Density and (b) pressure contours in analysis of inviscid free jet flow with uniform isotropic grid 61 × 61

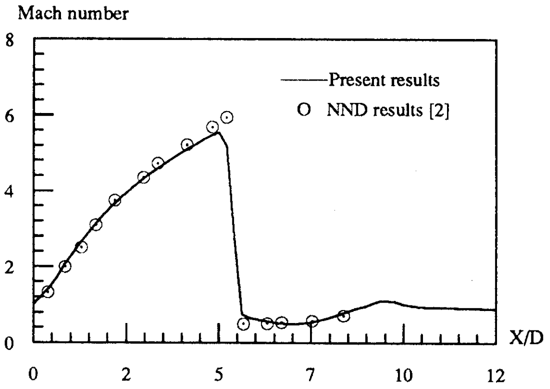

Figure 7. Mach number distribution along centreline of inviscid free jet flow

then

$$\left(\frac{\partial F^+}{\partial x}\right)_{im} = \textbf{minmod}\left[\left(\frac{\partial F^+}{\partial x}\right)_i, \left(\frac{\partial F^+}{\partial x}\right)_j\right], \qquad \left(\frac{\partial F^-}{\partial x}\right)_{jm} = \textbf{minmod}\left[\left(\frac{\partial F^-}{\partial x}\right)_i, \left(\frac{\partial F^-}{\partial x}\right)_j\right]. \tag{5}$$

Finally the expression of F is given as

$$F = F_i^+ + F_j^- + (x - x_i)\left(\frac{\partial F^+}{\partial x}\right)_{im} + (x - x_j)\left(\frac{\partial F^-}{\partial x}\right)_{jm}. \tag{6}$$

Substituting (6) into (2), we get the present discretized finite element algorithm which is accurate to second order.

For the N–S equation the viscous term and the source term may still be discretized by the classical Galerkin finite element method.

It can be proven that if the mass matrix of the left-hand term of (2) is replaced by a lumped diagonal mass matrix,[7] the present algorithm is reduced to the same form as the NND scheme.

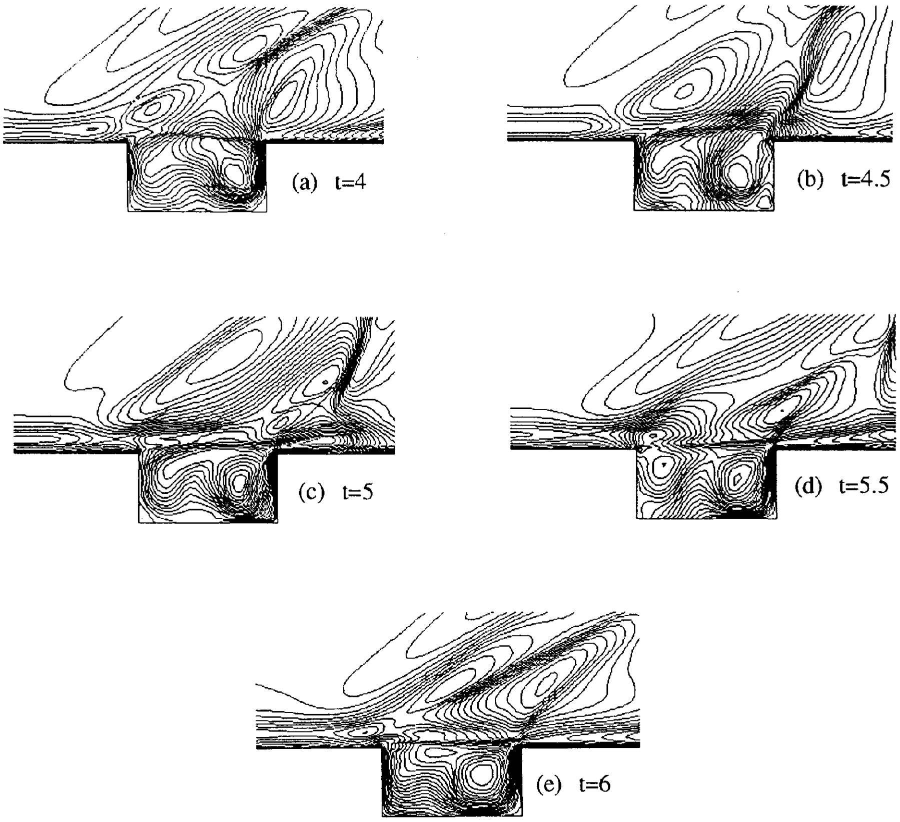

Figure 8. Density contours at various times for 2D cavity

3. EXTENSION OF NNFEM TO MULTIDIMENSIONAL EULER EQUATIONS

3.1. Discretization of 2D and axisymmetric Euler Equations

The 2D and axisymmetric Euler equations may be written in the form

$$\frac{\partial(y^{\varepsilon}U)}{\partial t}+\frac{\partial(y^{\varepsilon}F)}{\partial x}+\frac{\partial(y^{\varepsilon}G)}{\partial y}+\varepsilon K=0,$$

$$\varepsilon=\begin{cases}0, & \text{2D case,}\\ 1, & \text{axisymmetric case,}\end{cases} \tag{7}$$

$$U=\begin{bmatrix}\rho\\ \rho u\\ \rho v\\ e\end{bmatrix},\qquad F=\begin{bmatrix}\rho u\\ \rho u^2+p\\ \rho uv\\ (e+p)u\end{bmatrix},\qquad G=\begin{bmatrix}\rho v\\ \rho vu\\ \rho v^2+p\\ (e+p)v\end{bmatrix},\qquad K=\begin{bmatrix}0\\0\\0\\p\\0\end{bmatrix}.$$

For a quadrilateral element, after isoparametric transformation, equation (7) gives the form (Figure 1)

$$\frac{\partial(y^{\varepsilon}JU)}{\partial t}+\frac{\partial(y^{\varepsilon}J\tilde{F})}{\partial\xi}+\frac{\partial(y^{\varepsilon}J\tilde{G})}{\partial\eta}+\varepsilon JK=0, \tag{8}$$

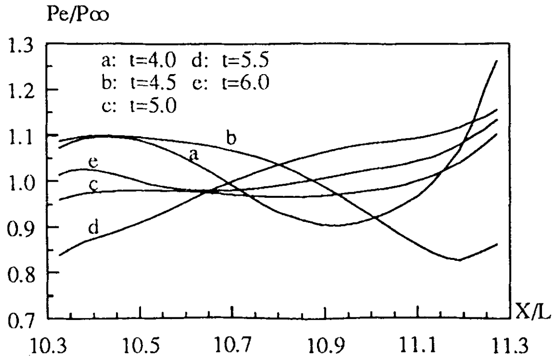

Figure 9. Pressure distribution along month of 2D cavity

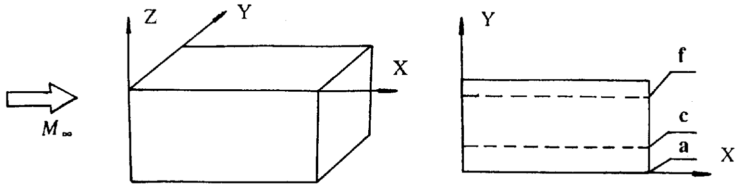

Figure 10. Geometric 3D cavity

where J is the determinant of the Jacobian matrix, $J = x_\xi y_\eta - x_\eta y_\xi$ and

$$\tilde{F} = F\xi_x + G\xi_y, \qquad \tilde{G} = F\eta_x + G\eta_y.$$

Applying Steger's flux-splitting technique, we get

$$\tilde{F} = \tilde{F}^+ + \tilde{F}^-, \qquad \tilde{G} = \tilde{G}^+ + \tilde{G}^-.$$

Then we should calculate the derivatives of positive and negative fluxes on each node and give the weighted integral of (7) in the form

$$\int [N][N]^{\mathrm{T}}\left[\frac{\partial U}{\partial t}\right] y^{\varepsilon} J \,\mathrm{d}\xi \mathrm{d}\eta = \int \frac{\partial [N]}{\partial \xi} y^{\varepsilon} J \tilde{F} \,\mathrm{d}\xi \mathrm{d}\eta + \int \frac{\partial [N]}{\partial \eta} y^{\varepsilon} J \tilde{G} \,\mathrm{d}\xi \mathrm{d}\eta - \varepsilon \int [N] J K \,\mathrm{d}\xi \mathrm{d}\eta - \int_L y^{\varepsilon} [N](F n_x + G n_y)\,\mathrm{d}l,$$

where the last term is a line integral along the boundary of the computational domain and n_x and n_y are the components of the vector perpendicular to the boundary.

Similarly to the 1D analysis, Taylor series expansion are applied for $\tilde{F}^{\pm}$ and $\tilde{G}^{\pm}$ to second-order accuracy. For example, the expression for $\tilde{F}^{\pm}$ associated with the node i can be written as (Figure 1)

$$\tilde{F} = \tilde{F}_L^+ + (1+\xi)\left(\frac{\partial \tilde{F}^+}{\partial \xi}\right)_L + (1+\eta)\left(\frac{\partial \tilde{F}^+}{\partial \eta}\right)_L + \tilde{F}_i^- + (\xi - 1)\left(\frac{\partial \tilde{F}^-}{\partial \xi}\right)_i + (1+\eta)\left(\frac{\partial \tilde{F}^-}{\partial \eta}\right)_i. \qquad (9)$$

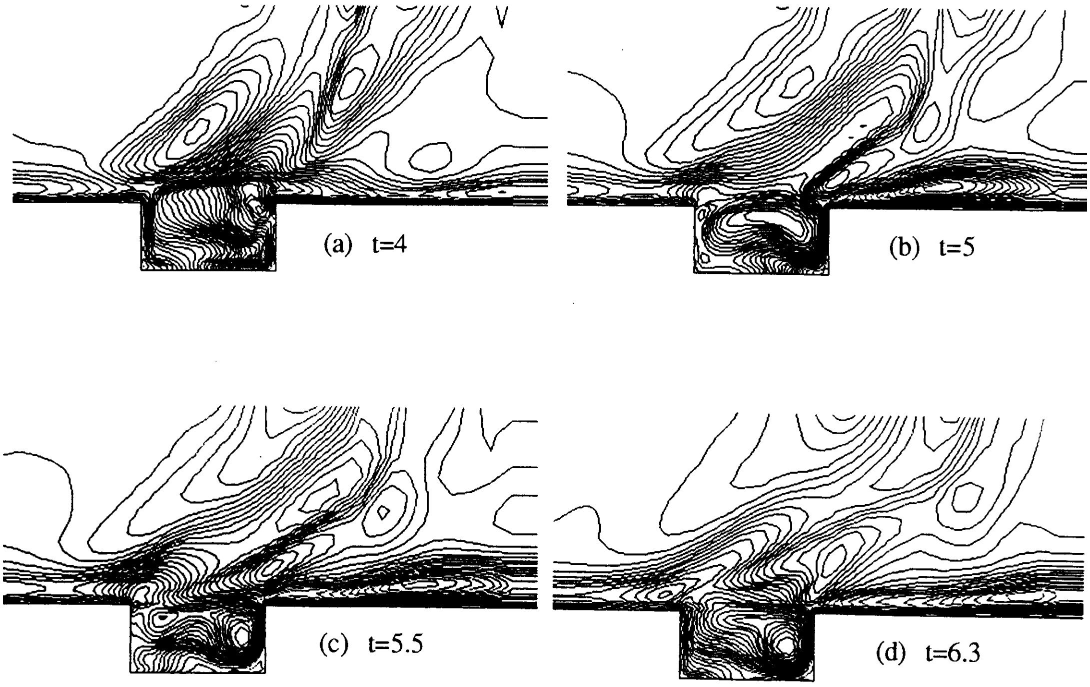

Figure 11. Density contours in symmetric section at various times

Since the coefficients of flux derivatives are regarded as first-order quantities, the expressions of flux derivatives need only first-order accuracy in order to keep $\tilde{F}$ at second-order accuracy. The derivatives along ξ and η are determined in the following way:

$$\left(\frac{\partial \tilde{F}^{+}}{\partial \xi}\right)_{L} = \frac{\tilde{F}_i^{+} - \tilde{F}_L^{+}}{2}, \qquad \left(\frac{\partial \tilde{F}^{-}}{\partial \xi}\right)_{i} = \frac{\tilde{F}_i^{-} - \tilde{F}_L^{-}}{2}, \qquad \left(\frac{\partial \tilde{F}^{+}}{\partial \eta}\right)_{L} = \frac{\tilde{F}_j^{+} - \tilde{F}_i^{+}}{2}, \qquad \left(\frac{\partial \tilde{F}^{-}}{\partial \eta}\right) = \frac{\tilde{F}_j^{-} - \tilde{F}_i^{-}}{2}. \tag{10}$$

Applying the increasing entropy condition along the ξ-direction as given in (5), the function $\tilde{F}$ associated with the node i can be finally given as

$$\tilde{F} = \tilde{F}_L^{+} + \tilde{F}_i^{-} + (1+\xi)\left(\frac{\partial \tilde{F}^{+}}{\partial \xi}\right)_{Lm} + (\xi - 1)\left(\frac{\partial \tilde{F}^{-}}{\partial \xi}\right)_{im} + (1+\eta)\frac{\tilde{F}_j - \tilde{F}_i}{2}, \tag{11}$$

where

$$\left(\frac{\partial \tilde{F}^{+}}{\partial \xi}\right)_{Lm} = \text{minmod}\left[\left(\frac{\partial \tilde{F}^{+}}{\partial \xi}\right)_{L}, \left(\frac{\partial \tilde{F}^{+}}{\partial \xi}\right)_{i}\right], \qquad \left(\frac{\partial \tilde{F}^{-}}{\partial \xi}\right)_{im} = \text{minmod}\left[\left(\frac{\partial \tilde{F}^{-}}{\partial \xi}\right)_{L}, \left(\frac{\partial \tilde{F}^{-}}{\partial \xi}\right)_{i}\right]. \tag{12}$$

Similarly, we can write down the expressions of $\tilde{F}$ and $\tilde{G}$ for all four nodes of this element.

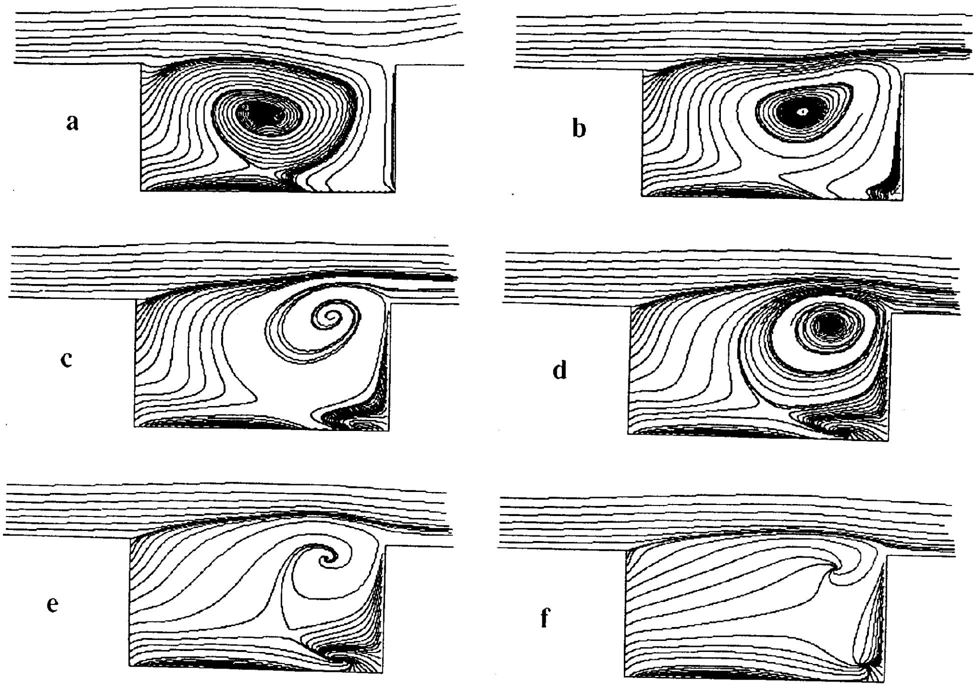

Figure 12. Streamline patterns in various sections at $t = 4$

3.2. Discretization of 3D Euler

For a hexahedral element (Figure 2), after isoparametric transformation, the 3D Euler equation gives the form

$$\frac{\partial(JU)}{\partial t} + \frac{\partial(J\tilde{F})}{\partial \xi} + \frac{\partial(J\tilde{G})}{\partial \eta} + \frac{\partial(J\tilde{H})}{\partial \zeta} = 0. \tag{13}$$

Repeating the deduction made in the 2D analysis, we can get the discretized expression of $\tilde{F}$ associated with the node i as

$$\tilde{F} = \tilde{F}_L^+ + \tilde{F}_i^- + (1+\xi)\left(\frac{\partial \tilde{F}^+}{\partial \xi}\right)_{Lm} + (\xi - 1)\left(\frac{\partial \tilde{F}^-}{\partial \xi}\right)_{im} + (1+\eta)\frac{\tilde{F}_j - \tilde{F}_i}{2} + (\zeta - 1)\frac{\tilde{F}_i - \tilde{F}_{i'}}{2}, \tag{14}$$

where the derivatives have the same forms as (10) and (12).

Similarly, we can write down the expressions of $\tilde{F}$, $\tilde{G}$ and $\tilde{H}$ for all eight nodes of the hexahedral element.

As for the time derivative term, it may be discretized using a lumped matrix technique[7] and takes the following for m with a second-order three-layer scheme at the time step $n+1$:

$$U^{n+1} = U^n + 0{\cdot}5\Delta t(3U_t^n - U_t^{n-1}). \tag{15}$$

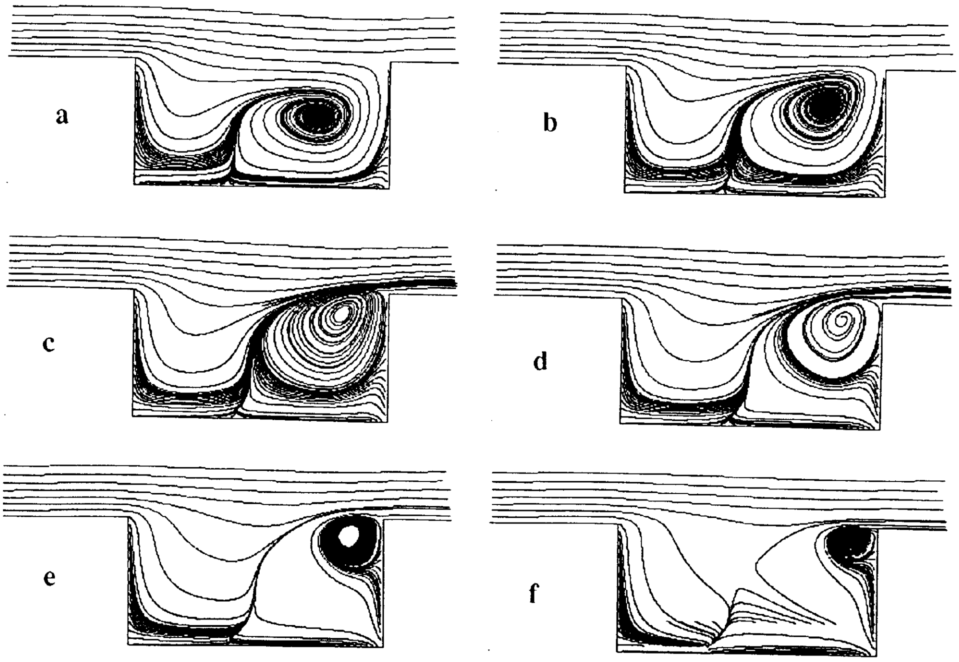

Figure 13. Streamline patterns in various sectrions at $t = 5$

4. APPLICATIONS OF NNFEM IN CFD

The present algorithm has been successfully checked in various cases: regular reflection of an oblique shock wave on a flat plate, supersonic flow over a forward step and axisymmetric free jet flow with a very high pressure ratio. It has also been applied with great success to the numerical study of supersonic flows over 2D and 3D rectangular cavities.

4.1. Inviscid oblique shock wave reflection

The first case computed is the regular reflection of an inviscid oblique shock wave ($\phi = 29^\circ$) on a flat plate with $M_\infty = 2{\cdot}9$ and a uniform isotropic grid of 121×31 points. Figures 3(a) and 3(b) show respectively the pressure contours and the pressure distribution along a grid line on $y = 0{\cdot}5$. No spurious oscillations were found in the shock wave region and the computational resolution for the shock wave is obviously better than that given by a first-order upwind scheme (Figure 3(c)).

4.2. Supersonic flow over a forward step

Based on the 2D N–S equations, the supersonic flow of $M_\infty = 2{\cdot}3$ over a forward step with the length–height ratio $L/H = 27{\cdot}7$ and $Re_{\infty,H} = 7200$ has been computed with the node number 16,400, where refinement of the grids is made just near the viscous wall. As shown in Figure 4, the graph of density contours results in good resolution in the whole flow field. The pressure distribution along the wall compares well with the experimental data of Reference 8, as seen in Figure 5.

Based on the Euler equations, the axisymmetric free jet flow in still air ($M_\infty = 0$) with the exit condition $M_j = 1$, the ratio of the surrounding pressure to the total exit pressure $p_\infty/p_{oj} = 1/50$ and the temperature ratio $T_\infty/T_{oj} = 1$ has been computed with the node number 61×61. It is well known that this was a difficult case for finite element simulation in the past because of the very strong shock

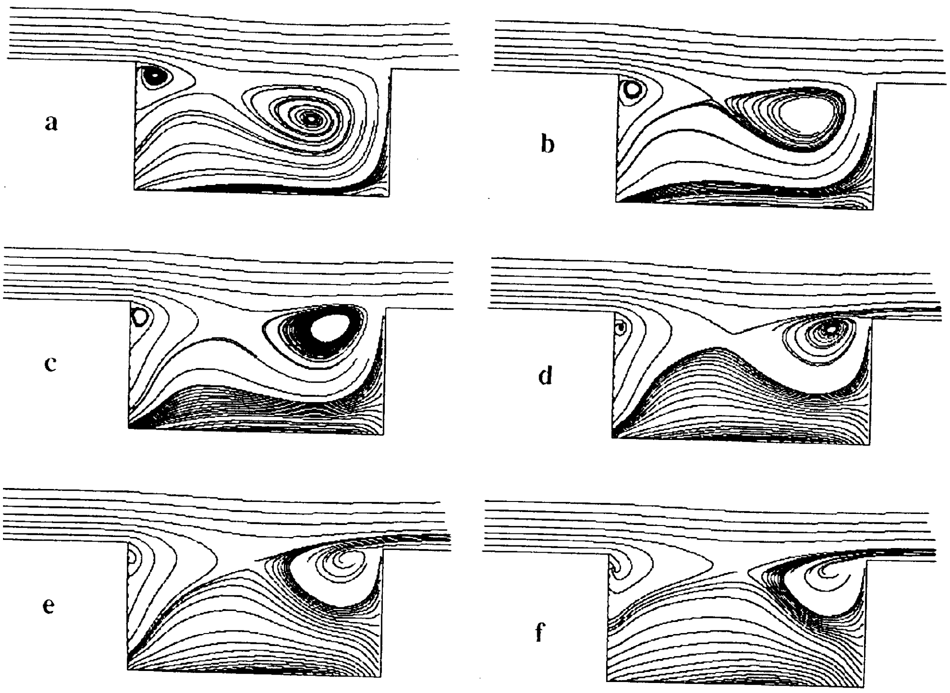

Figure 14. Streamline patterns in various sections at $t = 5{\cdot}5$

wave (Mach disc) involved. The density and pressure contours are shown in Figures 6(a) and 6(b) respectively, where we can clearly see a Mach disc located at a distance of about five exit diameters and the interaction between the Mach disc and a drum-like shock wave, which gives evidence of good computational resolution and no spurious oscillations across these shocks. Figure 7 shows the Mach number distribution along the centreline, which is in excellent agreement with the finite difference computational result of Reference 2.

4.3. Supersonic flow over a 2D rectangular cavity

Based on the N–S equations, the supersonic flow of $M_\infty = 1{\cdot}5$ over a 2D rectangular cavity with the length–height ratio $L/H = 2$ and $Re_{\infty,L} = 10^5$ has been predicted with the node number 61×31 in the cavity. The density contours of this flow at various times are shown in Figure 8, where we can clearly see the shock wave translating in a periodic motion and also the periodic vortex motion. Figure 9 shows the corresponding distributions along the bottom of the cavity. These phenomena are consistent with the experimental observations of Reference 9.

The supersonic flow of $M_\infty = 1{\cdot}5$ over a 3D rectangular cavity (Figure 10) with $L : H : W = 2 : 1 : 1$ and $Re_{\infty,L} = 105$ has been computed with the node number $31 \times 31 \times 15$ in the cavity. The density contours in the symmetric section of the cavity at various times are shown in Figure 11, where periodic motions of the shock wave and vortex flow, similar to the 2D case, can be detected. Figures 12–15 shown the streamline patterns of the cavity flow in its various sections at four time steps. We are not ready to discuss the flow physics in this paper, other than to note that it is a very complex unsteady separated and vortical flow with very interesting topological structures, including temporal changes in nodal points and saddle points and a transformation between separated and attached spiral points through limit cycles.

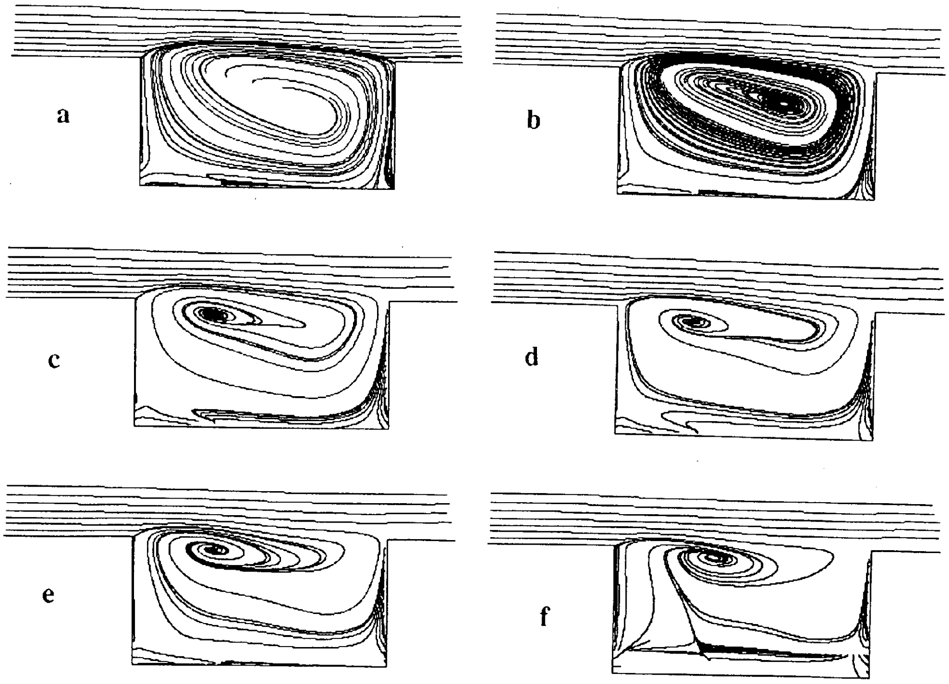

Figure 15. Streamline patterns in various sections at $t = 6{\cdot}3$

5. CONCLUSIONS

A non-oscillatory no-free-parameter finite element algorithm has been constructed on a physical basis, considering wave propagation characteristics in different characteristic directions across a strong discontinuity through flux splitting and Taylor series expansion in order to get a reasonable distribution of inviscid fluxes in every element and satisfy the increasing entropy condition. Its applications to steady and unsteady complex flows of shock wave interactions and massive separation with vortex motions have identified that the present algorithm gives good computational resolution without spurious oscillations in the shock wave region as well as in the whole flow field. Also, it is stable in operation and efficient in practice.

ACKNOWLEDGEMENTS

This study is supported by the National Natural Science Foundation of China. The authors are grateful to Dr. Bo-Nan Jiang for his valuable suggestions.

REFERENCES

1. A. Harten, ‘On a class of high resolution total variation-stable finite difference schemes’, *SIAM J. Anal.*, **21**, 1–23 (1984).
2. H. X. Zhang and F. G. Zhuang, ‘NND schemes and their applications to numerical simulation of two and three dimensional flows’, *Adv. Appl. Mech.*, **29**, 193–256 (1992).
3. T. J. R. Hughes and Mallet, ‘Recent progress in the development and understanding of SUPG methods with special reference to the compressible Euler and Navier–Stokes equations’, *Int. j. numer. methods fluids*, **7**, 1261–1275 (1987).
4. A. J. Baker and J. W. Kim, ‘Statement of algorithm for hypersonic conservation laws’, *Int. j. numer methods fluids*, **7**, 498–520 (1987).

5. R. Ramakrishman, K. S. Bey and E. A. Thorton, ‘An adaptive quadrilateral and triangular finite element scheme for compressible flows’, *AIAA Paper 88-0033*, 1988.
6. J. L. Steger and R. F. Warming, ‘Flux vector splitting of the inviscid gasdynamic equations with applications to finite difference methods’, *J. Comput. Phys.*, **40**, 263–293 (1981).
7. K. S. Bey and E. A. Thorton, ‘A new finite element approach for prediction of aerothermal and loads–progress in inviscid flow computations’, *NASA-TM-86434*, 1985.
8. D. R. Chapman, D. M. Kuehn and H. K. Larson, ‘Investigation of separated flows in supersonic and subsonic streams with emphasis on the effect of transition’, *NACA Rep. 1356*, 1958.
9. H. H. Heler and D. B. Bliss, ‘Aerodynamically induced pressure oscillations in cavities-physical mechanisms and suppression concepts’, *AFFDL-TR-74-13*, 1974.